

Ultra-High-*b*-Value Kurtosis Imaging for Noninvasive Tissue Characterization of Ovarian Lesions

Theresa Mokry, MD • Anna Mlynarska-Bujny • Tristan Anselm Kuder, Dr rer nat • Felix Christian Hasse, MD • Robert Hog, MD • Markus Wallwiener, Prof Dr • Christine Dinkic, MD • Janina Brucker, MD • Peter Simm, Prof Dr • Regula Gnirs • Hans-Ulrich Kauczor, Prof Dr • Heinz-Peter Schlemmer, Prof Dr • Joachim Rom, Prof Dr • Sebastian Bickelhaupt, MD

From the Department of Diagnostic and Interventional Radiology, Clinic of Diagnostic and Interventional Radiology, University Hospital Heidelberg, Im Neuenheimer Feld 110, 69120 Heidelberg, Germany (T.M., F.C.H., H.U.K.); Department of Radiology (T.M., A.M.B., R.H., R.G., H.P.S., S.B.) and Department of Medical Physics in Radiology (A.M.B., T.A.K.), German Cancer Research Center, Heidelberg, Germany; Medical Faculty Heidelberg, Heidelberg University, Heidelberg, Germany (A.M.B.); Hospital for General Obstetrics and Gynecology, University Hospital Heidelberg, Heidelberg, Germany (M.W., C.D., J.B.); Department of Pathology, Heidelberg University Hospital, Heidelberg, Germany (P.S.); Hospital for General Obstetrics and Gynecology, Frankfurt Hoechst, Germany (J.R.); Junior Group Medical Imaging and Radiology–Cancer Prevention, German Cancer Research Center, Heidelberg, Germany (R.H., S.B.); and Institute of Radiology, University Hospital Erlangen, Erlangen, Germany (S.B.). Received July 30, 2019; revision requested September 27; final revision received April 16, 2020; accepted April 30. Address correspondence to T.M. (e-mail: Theresa.mokry@med.uni-heidelberg.de).

Conflicts of interest are listed at the end of this article.

Radiology 2020; 296:358–369 • <https://doi.org/10.1148/radiol.2020191700> • Content codes:  

Background: MRI with contrast material enhancement is the imaging modality of choice to evaluate sonographically indeterminate adnexal masses. The role of diffusion-weighted MRI, however, remains controversial.

Purpose: To evaluate the diagnostic performance of ultra-high-*b*-value diffusion kurtosis MRI in discriminating benign and malignant ovarian lesions.

Materials and Methods: This prospective cohort study evaluated consecutive women with sonographically indeterminate adnexal masses between November 2016 and December 2018. MRI at 3.0 T was performed, including diffusion-weighted MRI (*b* values of 0–2000 sec/mm²). Lesions were segmented on *b* of 1500 sec/mm² by two readers in consensus and an additional independent reader by using full-lesion segmentations on a single transversal slice. Apparent diffusion coefficient (ADC) calculation and kurtosis fitting were performed. Differences in ADC, kurtosis-derived ADC (D_{app}), and apparent kurtosis coefficient (K_{app}) between malignant and benign lesions were assessed by using a logistic mixed model. Area under the receiver operating characteristic curve (AUC) for ADC, D_{app} , and K_{app} to discriminate malignant from benign lesions was calculated, as was specificity at a sensitivity level of 100%. Results from two independent reads were compared. Histopathologic analysis served as the reference standard.

Results: A total of 79 ovarian lesions in 58 women (mean age \pm standard deviation, 48 years \pm 14) were evaluated. Sixty-two (78%) lesions showed benign and 17 (22%) lesions showed malignant histologic findings. ADC and D_{app} were lower and K_{app} was higher in malignant lesions: median ADC, D_{app} , and K_{app} were 0.74 μ m²/msec (range, 0.52–1.44 μ m²/msec), 0.98 μ m²/msec (range, 0.63–2.12 μ m²/msec), and 1.01 (range, 0.69–1.30) for malignant lesions, and 1.13 μ m²/msec (range, 0.35–2.63 μ m²/msec), 1.45 μ m²/msec (range, 0.44–3.34 μ m²/msec), and 0.65 (range, 0.44–1.43) for benign lesions (*P* values of .01, .02, < .001, respectively). AUC for K_{app} of 0.85 (95% confidence interval: 0.77, 0.94) was higher than was AUC from ADC of 0.78 (95% confidence interval: 0.67, 0.89; *P* = .047).

Conclusion: Diffusion-weighted MRI by using quantitative kurtosis variables is superior to apparent diffusion coefficient values in discriminating benign and malignant ovarian lesions and might be of future help in clinical practice, especially in patients with contraindication to contrast media application.

© RSNA, 2020

Online supplemental material is available for this article.

Accurate characterization of ovarian lesions as benign or malignant is of high clinical relevance. Patients with ovarian cancer are best managed in specialist units. Patients with complete macroscopic cytoreduction at initial surgical procedure (residual tumor \leq 1 cm) have higher survival rates than do patients with more extensive residual disease, whereas benign lesions can be managed conservatively or with a minimally invasive surgical procedure (1–3).

US is the primary imaging modality in assessing ovarian masses (3). Reported accuracies for transvaginal US vary between 63% and 92% and are highly operator dependent (4–7). MRI is the imaging modality of choice to further assess sonographically indeterminate ovarian lesions (8,9). The accuracy of conventional MRI including T1-weighted,

T2-weighted, fat-suppressed, and contrast material-enhanced sequences ranges from 71% to 93% (10–13). Semiquantitative dynamic contrast-enhanced MRI further improves diagnostic performance, with reported accuracies of up to 100% (14,15).

In recent years, functional MRI techniques such as diffusion-weighted MRI have emerged. However, its diagnostic contribution for differentiating benign and malignant ovarian lesions remains controversial (16). Fujii et al (17) analyzed 123 ovarian lesions without excluding specific histologic findings and found no diagnostic benefit for diffusion-weighted MRI. Other groups have reported added benefit of diffusion-weighted MRI when excluding cystic teratomas and endometriomas (13).

Abbreviations

ADC = apparent diffusion coefficient, AUC = area under the receiver operating characteristic curve, CI = confidence interval, D_{app} = kurtosis-derived ADC, K_{app} = apparent kurtosis coefficient, SI = signal intensity

Summary

A diffusion-weighted MRI protocol using kurtosis variables allowed discrimination of benign and malignant ovarian lesions, with 55% (34 of 62) of benign lesions classified at a sensitivity level of 100%.

Key Results

- Apparent diffusion coefficient (ADC) and kurtosis-derived ADC were lower and apparent kurtosis coefficient (K_{app}) was higher in malignant compared with benign ovarian lesions (median values, $0.74 \mu\text{m}^2/\text{msec}$, $0.98 \mu\text{m}^2/\text{msec}$, and 1.01 vs $1.13 \mu\text{m}^2/\text{msec}$, $1.45 \mu\text{m}^2/\text{msec}$, and 0.65 ; P values of .01, .02, < .001, respectively).
- K_{app} had the highest area under the receiver operating characteristic curve of 0.85 for discriminating benign from malignant lesions.
- K_{app} correctly classified 55% (34 of 62) of benign lesions compared with 27% (17 of 62) for ADC ($P = .047$) prior to surgical procedure without compromising sensitivity.

The American College of Radiology Appropriateness Criteria state pelvic MRI without and with intravenous contrast agent “may be appropriate” for a suspected adnexal mass in pre- and postmenopausal women without acute symptoms at initial imaging. They describe a high accuracy rate of 95% in characterizing indeterminate adnexal lesions when combining qualitative and quantitative diffusion-weighted MRI, as well as perfusion-weighted MRI sequences (18). The 2016 European Society of Urogenital Radiology guidelines for MRI of sonographically indeterminate adnexal masses recommend diffusion-weighted MRI only as a problem-solving sequence for solid lesions or to assess solid components of cystic-solid lesions with low signal intensity (SI) on T2-weighted sequences to determine benignity (8).

Diffusion-weighted MRI assesses water molecule diffusive motion in tissues (19), where the apparent diffusion coefficient (ADC) is measured. It is assumed that a Gaussian distribution (20) can be used to describe the spin phases generated by diffusive motion. However, in biologic tissues, diffusion of water molecules is more complex due to cellular microstructural barriers (20,21), such as cytomembranes and extracellular matrix (22).

Diffusion kurtosis MRI, first described in 2005 (23), quantifies non-Gaussian water diffusivity (20) and may provide additional information on tissue heterogeneity, cellularity, and vascularity (20). In recent studies, diffusion kurtosis MRI has shown potential benefit in diagnosing prostate cancer (21), in discriminating benign and malignant breast lesions (24), in distinguishing histopathologic subtypes of rectal cancer (22), and in characterizing glioma (25).

However, there is limited evidence of its diagnostic value in differentiating benign from malignant ovarian lesions prior to surgical procedure. The purpose of our study was, therefore, to determine whether diffusion kurtosis MRI allows a more accurate differentiation in between malignant and benign ovarian lesions compared with ADC values in participants with sonographically indeterminate adnexal masses and if diffusion kurtosis variables in combination with conventional MRI show

potential in improving general performance of preoperative MRI evaluation.

Materials and Methods

No industry gave support specifically for this study. The authors had control of the data and the information within this article.

Study Participants

This prospective single-institutional cohort study was approved by our institutional ethics review board (S-337/2016) and written informed consent was obtained from all participants. Between November 2016 and December 2018, potentially eligible adult participants with sonographically indeterminate adnexal masses were identified following transvaginal US in the gynecology department of our hospital. Exclusion criteria were denial of participation, general contraindications to MRI, and inability to consent. Figure 1 summarizes the study flowchart, and Table 1 details participants' characteristics. All included participants underwent surgical procedure and resected masses were sent for histopathologic analysis.

Histopathologic Analysis

Histopathologic analysis served as reference standard for all lesions of the analyzed cohort. Analysis was performed by two pathologists in consensus, at least one of whom had more than 10 years of experience. In case of disagreement, consensus was reached by arbitration (possibly involving more than two pathologists). The majority (>70%) were seen by two pathologists who specialized in gynecologic pathology.

MRI Examinations

All MRI examinations were performed with a 3.0-T MRI scanner (Prisma; Siemens, Erlangen, Germany) with a 16-channel body coil and consisted of a full diagnostic protocol, including morphologic sequences, diffusion-weighted MRI, and (if not declined by the participant) dynamic contrast-enhanced sequences (Prohance; Bracco, Milan, Italy) (Table E1 [online]).

The diffusion-weighted MRI sequence was acquired prior to contrast agent administration to avoid potential influence of gadolinium-based contrast agent on the diffusion-weighted MRI signal and contained six different b values (0, 50, 100, 800, 1500, and 2000 sec/mm^2). Imaging time for the diffusion-weighted sequence alone was 10 minutes 23 seconds for 60 slices. In six participants, the extensive size of the lesion required additional slices to cover the whole lesion.

Reading of the Full Diagnostic Protocol (All Standard Sequences including Time-Intensity Curves)

The initial diagnostic examination was read by a radiology resident and a radiology attending in consensus, and then finalized by the senior radiology attending specializing in gynecologic radiology (T.M., with 8 years of experience in pelvic MRI). Image analysis followed the algorithmic approach suggested by Forstner et al (8) in the European Society of Urogenital Radiology guideline on sonographically indeterminate adnexal masses. The report was finalized prior to surgical procedure

and before analysis of diffusion kurtosis MRI was performed. Therefore, the readers were blinded to histopathologic and kurtosis analysis.

Imaging Analysis for Diffusion-weighted and Diffusion Kurtosis MRI

All diffusion-weighted MR images were transferred to a standard personal computer for postprocessing with open-source software (version 2018.04.2, Medical Image Interaction Toolkit; German Cancer Research Center, Heidelberg, Germany) (26). Two board-certified radiologists (T.M. and S.B. [with 7 years of MRI experience]) read the images concurrently in consensus. The image containing that part of the lesion with the highest SI qualitatively on high-*b*-value images (1500 sec/mm²) was identified and the lesion was outlined manually on this single slice (Fig 2). In some cases (*n* = 13), *b* of 800 sec/mm² images were used additively to support delineation of lesion boundaries. T2-weighted images were made available on a separate picture archiving and communication system workstation to identify the lesion, because diffusion-weighted MRI alone did not always provide sufficient morphologic information. At the time of image analysis, readers were blinded to histopathologic results. To ensure reproducibility, a second independent read and segmentation of the lesions as described above were performed by a radiology resident with 3 years of MRI experience. Only diffusion-weighted and T2-weighted images were made available for this.

ADC Calculation and Kurtosis Fitting

By using a curve-fitting algorithm based on the functions from the official Matlab Curve Fitting Toolbox (version R2016a; MathWorks, Natick, Mass), the following diffusion variables were quantified.

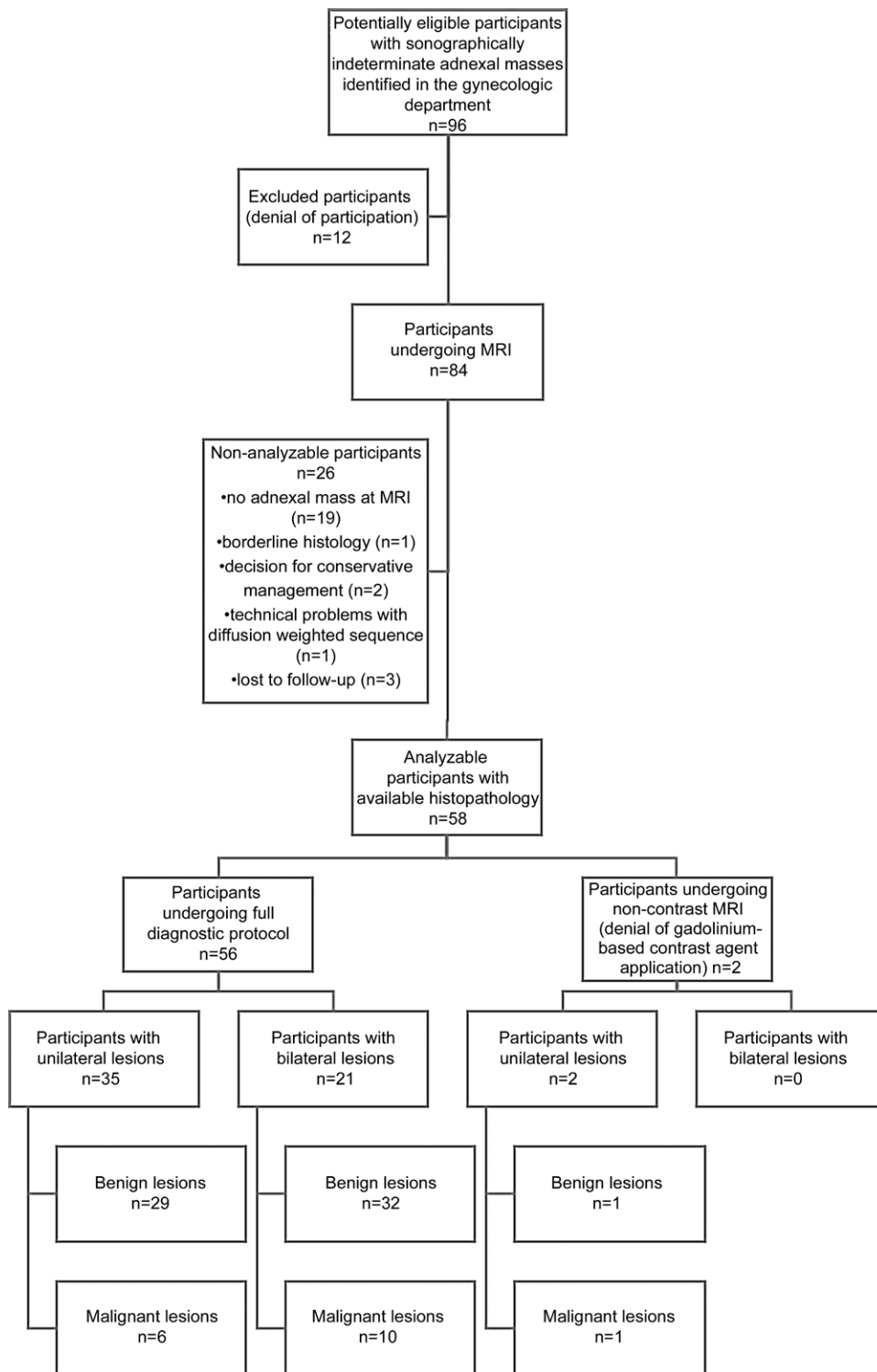


Figure 1: Flowchart shows participant selection.

The ADC maps were calculated by using a monoexponential fit to the measured signal:

$$S(b) = S_0 \cdot e^{(-b \cdot ADC)}$$

where $S(b)$ is diffusion-weighted signal, b is the strength of diffusion weighting, and S_0 is the non-diffusion-weighted signal.

Table 1: Participant and Lesion Characteristics

Characteristic	No. of Findings	Benign Lesions (62 in 46 Participants)	Malignant Lesions (17 in 12 Participants)
Participant			
Mean age (y)*	...	46 ± 14	56 ± 11
Sex	...		
Female	...	100 (46/46)	100 (12/12)
Male	...	0 (0/46)	0 (0/12)
Menopausal status at diagnosis	...		
Premenopausal	...	56.5 (26/46)	41.7 (5/12)
Perimenopausal	...	4.3 (2/46)	16.7 (2/12)
Postmenopausal	...	39.1 (18/46)	41.7 (5/12)
Clinical symptoms	...		
Yes	...	32.6 (15/46)	66.7 (8/12)
No	...	67.4 (31/46)	33.3 (4/12)
Lesion			
Diameter (cm)	...		
Mean†	...	7.4 (2.7–25.9)	9.5 (4.6–14.0)
Median	...	5.9	10.5
Morphology‡			
Predominantly cystic§	37	59.7 (37/62)¶	0 (0/17)
Cystic-solid#	34	30.1 (19/62)	88.2 (15/17)
Predominantly solid or purely solid**	8	9.7 (6/62)	11.8 (2/17)
Bilaterality (%)	21	25.8 (16/62)	29.4 (5/17)
Part with high signal intensity on $b = 1500 \text{ sec/mm}^2$ (%)	66	79.0 (49/62)	100 (17/17)
Time–signal intensity curve (%)†††			
Type 1	31	79.5 (31/31)	0 (0/31)
Type 2	13	20.5 (8/13)	31.3 (5/13)
Type 3	11	0 (0/11)	68.8 (11/11)

Note.—Unless otherwise specified, data are percentages, with numerators and denominators in parentheses.

* Data are mean ± standard deviation; $P = .06$.

† Data in parentheses are the minimum and maximum; $P = .01$.

‡ Assessed at MRI.

§ Unilocular or multilocular cystic with septa but without truly solid components.

¶ Twenty-three were predominantly hemorrhagic (22 endometriomas, one mucinous cystadenoma).

Mixed cystic-solid lesion with at least one truly solid portion.

** Mixed lesion with very little cystic parts, if any.

†† Imaging analysis after gadolinium-based contrast agent administration according to European Society of Urogenital Radiology guidelines. Source.—Reference 8.

††† Twenty-two lesions did not show intralesional contrast enhancement and two patients declined contrast media administration, so 24 lesions were excluded from time–signal intensity curve analysis.

The ADC was calculated by using three b values: 100, 800, and 1500 sec/mm^2 . The signal obtained with very low and high b values was not used during the fitting process to reduce the effects of perfusion at the lower b values and of non-Gaussian diffusion at higher b values.

Diffusion kurtosis MRI variables, D_{app} and K_{app} , were obtained by using a nonlinear fit of the following equation:

$$S(b) = S_0 \cdot e^{\left(-b \cdot D_{\text{app}} + \frac{1}{6} b^2 D_{\text{app}}^2 K_{\text{app}}\right)},$$

where $S(b)$ again represents the diffusion-weighted signal, S_0 is the signal with $b = 0$, D_{app} is the diffusion kurtosis MRI–derived

ADC, and K_{app} is the apparent kurtosis coefficient. The b values 100, 800, 1500, and 2000 sec/mm^2 were used. Again, the low b values were excluded to diminish the influence of perfusion effects (intravoxel incoherent motions) (27). $S(b = 0)$ was taken as a starting point for the fit variable S_0 . The D_{app} differs from ADC due to the use of the modified fitting function to simultaneously estimate diffusion coefficient and kurtosis and the use of different b values. As a result of the separation of kurtosis effects in the fitting equation, D_{app} is usually larger than ADC.

To select the most substantial voxels for the quantitative analysis, using Matlab, we determined the 10% and 1% of voxels with the highest SI, respectively. The selection was based on literature suggesting that voxels with the highest amount of diffusion

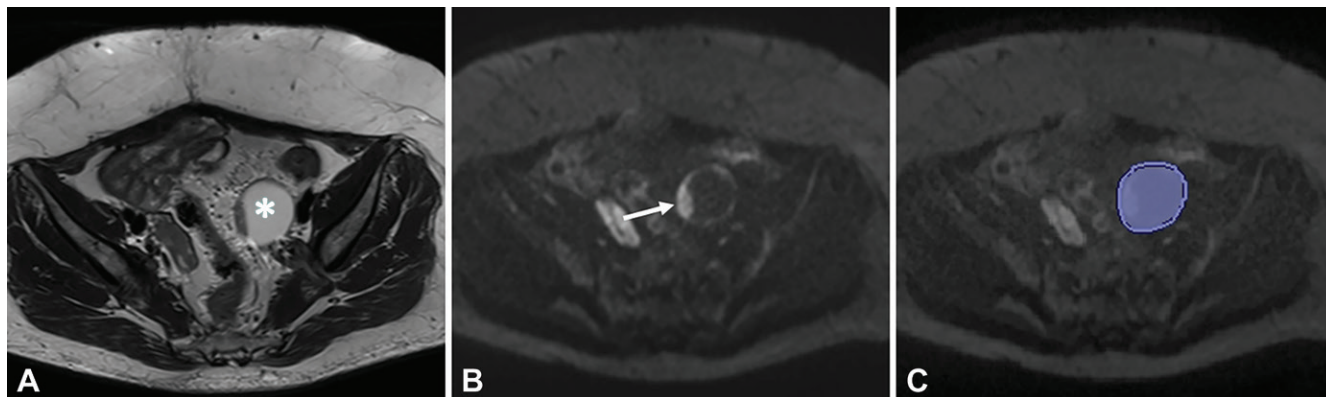


Figure 2: Images in a 51-year-old woman with fibroma of left ovary. A, Transversal T2-weighted MR image (repetition time msec/echo time msec, 5170/78) shows mixed cystic-solid lesion (*). B, Transversal diffusion-weighted MR image (9200/59) obtained at $b = 1500 \text{ sec/mm}^2$ shows high signal intensity of solid tissue (arrow). C, Same image with manual segmentation (blue region of interest) of entire lesion on selected transversal slice.

restriction were most suitable to differentiate between malignant and benign lesions in varying organs (28–32) with the 10th percentile and minimum voxels being most commonly selected and further being suggested to represent the most aggressive parts of malignant lesions (33).

Owing to the fact that ovarian lesions can include large portions of cystic or liquid content, we analyzed both the 10% and 1% of voxels with the highest SI. However, at least 11 voxels were kept to ensure a sufficient number of voxels in small lesions. This lower limit was based on published literature (34,35).

Initially, voxels within the b of 1500 sec/mm^2 image were sorted according to their SI. Then, an SI threshold was defined as a minimum SI value among the predefined percentage (10% or 1%) of the voxels with the highest intensity. Finally, the voxels with the SI higher than the threshold were selected. If lesions showed a high number of voxels at the absolute threshold level, which would lead to the inclusion of overall more than 1% or 10% voxels of a lesion, then the number of voxels included at this threshold was reduced until the 1% or 10% level was reached.

For quantitative analyses, ADC and D_{app} values were required to be within the range of $0\text{--}3.5 \mu\text{m}^2/\text{msec}$. K_{app} values were selected to be within the range of values of $0\text{--}3$. All voxels outside of these chosen intervals were excluded from the following analysis of data. The boundaries of diffusion-weighted and diffusion kurtosis MRI-derived variables were selected to exclude significant outliers caused by artifacts, which might be related to flow or motion within the voxel.

During analysis, the expected ADC value for free water of $3.25 \mu\text{m}^2/\text{msec}$ was chosen as the upper limit of the ADC, while the upper limit of apparent kurtosis coefficient values was based on current values suggested by the literature on kurtosis imaging (36–38). Finally, only the voxels satisfying the following conditions were included: 0 less than ADC less than $3.5 \mu\text{m}^2/\text{msec}$ for ADC analysis and 0 less than K_{app} less than 3.0 for diffusion kurtosis MRI. However, if the final number of the chosen voxels was smaller than 11, then the SI threshold was decreased and the whole procedure was repeated until the number of 11 selected voxels was reached. Table E2 (online) summarizes the final fraction of the voxels used for calculations.

Reading of Conventional MRI (All Standard Sequences Excluding Time-Intensity Curves) in Combination with Diffusion Kurtosis Imaging

Following on from diffusion-weighted MRI analysis, an additional read was performed by the same readers (T.M. and S.B.), who analyzed the conventional MRI sequences including the contrast-enhanced sequences but without the time-intensity curves for evaluation purposes.

Additionally, for the lesions determined visually as malignant, the kurtosis cutoff was then used to assess the potential of the method to reduce false-positive results. The time interval between this read and the read of the full diagnostic protocol was greater than 2 months to minimize recall bias.

Reading of Full Diagnostic Protocol in Combination with Diffusion Kurtosis Imaging

The same was performed for the full diagnostic protocol by the same readers (T.M. and S.B.). Again, the kurtosis cutoff was used to assess its potential to reduce false-positives for lesions determined malignant when reading the full diagnostic protocol including time-intensity curves.

Statistical Analysis

The statistical analysis was performed by using Matlab (version 2016b; Mathworks), SigmaPlot (version 14.0; Systat Software, San Jose, Calif), and SAS (version 3.71; SAS Institute, Cary, NC). Median values of each variable were calculated. The number of voxels in the region of interest was analyzed and compared between different lesions by using the Mann-Whitney U test after normality testing with the Shapiro-Wilk test. The statistical significance of differences in the derived variables was calculated by using a linear mixed model (Glimmix in SAS) to address the potential correlation of multiple lesions detected in individual patients.

The ability to discriminate malignancy from benignity was assessed by using receiver operating characteristic curves based on a logistic mixed model (Glimmix in SAS) with a single variable. Subsequently, a logistic mixed model with two predictors was used to assess an added benefit of variable combination. The statistical significance of differences in the area under the receiver

Table 2: Histologic Results of Examined Ovarian Lesions

Histologic Result	Total No.
Benign (n = 62)	
Cystadenoma	
Serous	4
Mucinous	5
Cystadenofibroma	
Serous	10
Mucinous	5
Seromucinous	1
Fibroma	3
Benign transitional cell tumor (Brenner tumor)	2
Endometrioma	18
Dermoid (mature cystic teratoma)	4
Corpus luteal cyst (hemorrhagic)	7
Fibroblastic tissue	1
Necrotic pseudoxanthomatic nodule	1
Mucinous cystadenofibroma with associated mature teratoma	1
Malignant (n = 17)	
Ovarian carcinoma	
Serous (high grade)	9
Mucinous	1
Endometrioid	2
Granulosa cell tumor	1
Ovarian metastasis	3
Squamous cell carcinoma arising in monodermal teratoma	1

operating characteristic curve (AUC) was tested by using the DeLong, DeLong, and Clarke-Pearson method. For all tests, P values $\leq .05$ were considered to indicate statistical significance.

To test reliability, the intraclass correlation coefficients and their 95% confident intervals (CIs) were calculated based on a single-rating, absolute agreement, two-way mixed-effects model. An intraclass correlation coefficient value of less than 0.5 was indicative of poor reliability, 0.5–0.75 of moderate reliability, 0.75–0.9 of good reliability, and greater than 0.9 of excellent reliability (39). AUCs were compared by using the DeLong, DeLong, and Clarke-Pearson method.

Statistical comparisons of the performance of the full diagnostic protocol versus conventional MRI plus diffusion kurtosis imaging and full diagnostic protocol versus diffusion kurtosis imaging alone were performed by using McNemar test.

Results

Study Participants

Ninety-six women with sonographically indeterminate adnexal masses were identified as eligible in the gynecologic department of our hospital. Twelve denied participation, so 84 women were included and underwent MRI. Another 26 participants were nonanalyzable; for further details, see Figure 1.

Eventually, 79 ovarian lesions in 58 women (mean age \pm standard deviation, 48 years \pm 14; range, 24–77 years) were

analyzed (participant and lesion characteristics are shown in Table 1).

Histopathologic Results

Of the 79 lesions analyzed, 62 (78%) showed a benign histologic finding, whereas 17 (22%) lesions were malignant. Histopathologic results are shown in Table 2. The mean time interval between MRI and surgical procedure and histopathologic analysis was 41.7 days (range, 1–204 days). Cases with longer intervals than 8 weeks were due to patient's decision of postponing surgical procedure and all had benign histologic results: seven patients with endometrioma (range, 75–204 days) and three patients with cystadenoma or cystadenofibroma (range, 114–160 days).

Diagnostic Performance of Diffusion-weighted MRI and Diffusion Kurtosis MRI–derived Variables

Results for analysis of 1% and 10% of region-of-interest voxels are presented in Table 3 and Figure 3, respectively. Results for the second independent reader are shown in Table E3 (online).

The median number of voxels used for the 1% analysis was 14 voxels (range, 11–121 voxels) versus 23 voxels (range, 11–84 voxels; $P = .01$) for benign versus malignant lesions, respectively, for the monoexponential fitting model; and 13 voxels (range, 11–119 voxels) versus 23 voxels (range, 11–84 voxels; $P = .01$) for benign versus malignant lesions, respectively, for diffusion kurtosis MRI.

The median number of voxels used for the 10% analysis was 117.5 voxels (range, 31–1160 voxels) versus 235 voxels (range, 17–889 voxels; $P = .01$) for benign versus malignant lesions, respectively, for the monoexponential fitting model; and 97 voxels (range, 12–1035 voxels) versus 233 voxels (range, 17–885 voxels; $P = .002$) for benign versus malignant lesions, respectively, for diffusion kurtosis MRI.

When analyzing 1% of voxels, median ADC was higher for benign than malignant lesions: $1.13 \mu\text{m}^2/\text{msec}$ (range, 0.35– $2.63 \mu\text{m}^2/\text{msec}$) versus $0.74 \mu\text{m}^2/\text{msec}$ (range, 0.52– $1.44 \mu\text{m}^2/\text{msec}$) with an average difference after additive generalized linear mixed model, or GLMM, modeling of -0.45 (95% CI: -0.78 , -0.11 ; $P < .01$). For diffusion kurtosis MRI, median D_{app} was also higher for benign than malignant lesions: $1.45 \mu\text{m}^2/\text{msec}$ (range, 0.44– $3.34 \mu\text{m}^2/\text{msec}$) versus $0.98 \mu\text{m}^2/\text{msec}$ (range, 0.63– $2.12 \mu\text{m}^2/\text{msec}$) with an average difference after additive GLMM modeling of -0.55 (95% CI: -0.98 , -0.12 ; $P = .02$). Median K_{app} was lower for benign than malignant lesions: 0.65 (range, 0.44–1.43) versus 1.01 (range, 0.69–1.30; $P < .001$).

When analyzing 10% of voxels, median ADC was higher for benign than malignant lesions: $1.38 \mu\text{m}^2/\text{msec}$ (range, 0.41– $2.81 \mu\text{m}^2/\text{msec}$) versus $0.82 \mu\text{m}^2/\text{msec}$ (range, 0.51– $1.68 \mu\text{m}^2/\text{msec}$) with an average difference after additive GLMM modeling of -0.56 (95% CI: -0.93 , -0.18 ; $P < .01$). For diffusion kurtosis MRI, median D_{app} was also higher for benign than malignant lesions: $1.80 \mu\text{m}^2/\text{msec}$ (range, 0.52– $3.39 \mu\text{m}^2/\text{msec}$) versus $1.07 \mu\text{m}^2/\text{msec}$ (range, 0.66– $2.24 \mu\text{m}^2/\text{msec}$) with an average difference after additive GLMM modeling of -0.62 (95% CI: -1.02 , -0.21 ; $P = .01$). Median K_{app} was lower for benign than malignant lesions: 0.62 (range, 0.40–1.55) versus 0.86 (range, 0.57–1.28; $P = .004$).

Table 3: Summary of the Variables Derived by Using Diffusion and Kurtosis Diffusion Model

Variable	Benign	Malignant	Statistical Analysis Derived by Using Linear Mixed Model		
			Average Difference	95% Confidence Interval	P Value
1% analysis					
ADC ($\mu\text{m}^2/\text{msec}$)			−0.45	−0.78, −0.11	.01
Median	1.13	0.74			
Minimum-maximum	0.35–2.63	0.52–1.44			
D_{app} ($\mu\text{m}^2/\text{msec}$)			−0.55	−0.98, −0.12	.02
Median	1.45	0.98			
Minimum-maximum	0.44–3.34	0.63–2.12			
K_{app}			0.27	0.14, 0.41	<.001
Median	0.65	1.01			
Minimum-maximum	0.44–1.43	0.69–1.30			
10% analysis					
ADC ($\mu\text{m}^2/\text{msec}$)			−0.56	−0.93, −0.18	.01
Median	1.38	0.82			
Minimum-maximum	0.41–2.81	0.51–1.68			
D_{app} ($\mu\text{m}^2/\text{msec}$)			−0.62	−1.02, −0.21	.01
Median	1.80	1.07			
Minimum-maximum	0.52–3.39	0.66–2.24			
K_{app}			0.21	0.07, 0.34	.004
Median	0.62	0.86			
Minimum-maximum	0.40–1.55	0.57–1.28			

Note.—ADC = apparent diffusion coefficient, D_{app} = kurtosis-derived ADC, K_{app} = apparent kurtosis coefficient.

Receiver operating characteristic curves for both 1% and 10% analyses are shown in Figure 4. The diagnostic performance of the variables is summarized in Table 4. Analysis after GLMM modeling showed the highest AUC value for K_{app} of 0.85 for both 1% and 10% analyses (for 1%, 95% CI: 0.77, 0.94; for 10%, 95% CI: 0.75, 0.95) while the AUC for ADC was 0.78 (95% CI: 0.67, 0.89) for 1% analysis and 0.80 (95% CI: 0.70, 0.91) for 10% analysis, respectively, and D_{app} was 0.77 (95% CI: 0.66, 0.89) for 1% analysis and 0.80 (95% CI: 0.69, 0.91), respectively.

The differences in AUC between K_{app} and ADC variables were statistically significant for the 1% analysis ($P = .047$), but not for the 10% analysis ($P = .06$). The differences in AUC between D_{app} and K_{app} were not significant ($P > .05$). By using a sensitivity threshold of 100%, a correct classification of the indeterminate lesions as benign occurred for 27% (95% CI: 0.17, 0.40) using ADC, 21% (95% CI: 0.12, 0.33) using D_{app} , and 55% (95% CI: 0.42, 0.68) using K_{app} (1% analysis), and for 29% (95% CI: 0.18, 0.42) using ADC, 29% (95% CI: 0.18, 0.42) using D_{app} , and 32% (95% CI: 0.21, 0.45) using K_{app} (10% analysis). Combining K_{app} with D_{app} and K_{app} with ADC by building logistic mixed models with two predictors, respectively, did not significantly improve specificity.

Intraclass correlation coefficient estimation revealed good to excellent interreader agreement for all parameters: within the 1% analysis 0.884 (95% CI: 0.824, 0.924) for ADC, 0.893 (95% CI: 0.838, 0.930) for D_{app} , and 0.838 (95% CI: 0.758, 0.893) for K_{app} ; within the 10% analysis 0.946 (95% CI: 0.9161, 0.965) for ADC, 0.939 (95% CI: 0.906, 0.961) for D_{app} , and 0.884

(95% CI: 0.825, 0.924) for K_{app} . Detailed numbers and AUC for the second independent read for both 1% and 10% analyses are shown in Tables E4 and E5 (online). Receiver operating characteristic curves of reader 2 are shown in Figure E1 (online).

Diagnostic Performance of Full Diagnostic Protocol

Reading the full diagnostic protocol, all 17 (100%; 95% CI: 80.5%, 100%) malignant lesions were correctly classified as malignant, whereas 55 of 62 (88.7%; 95% CI: 78.1%, 95.3%) benign lesions were correctly assessed as benign prior to surgical procedure. The remaining seven benign lesions (11.3%; 95% CI: 4.7%, 21.9%) were evaluated as borderline or malignant, or remained indeterminate after MRI examination.

Adding Diffusion Kurtosis Imaging to the Full Diagnostic Protocol

If the readers would have used the quantitative kurtosis cutoff for all lesions considered malignant by the full diagnostic protocol, of the seven false-positive lesions from reading the full diagnostic protocol, diffusion kurtosis analysis would have correctly classified five as benign while preserving a sensitivity of 100%. The combination of a full diagnostic protocol and diffusion kurtosis MRI theoretically could thus have correctly classified 60 of 62 (96.8%; 95% CI: 88.8%, 99.6%) benign lesions.

Diagnostic Performance of Conventional MRI

By reading the conventional MRI with contrast enhancement but without time-intensity curves, all 17 (100%; 95%

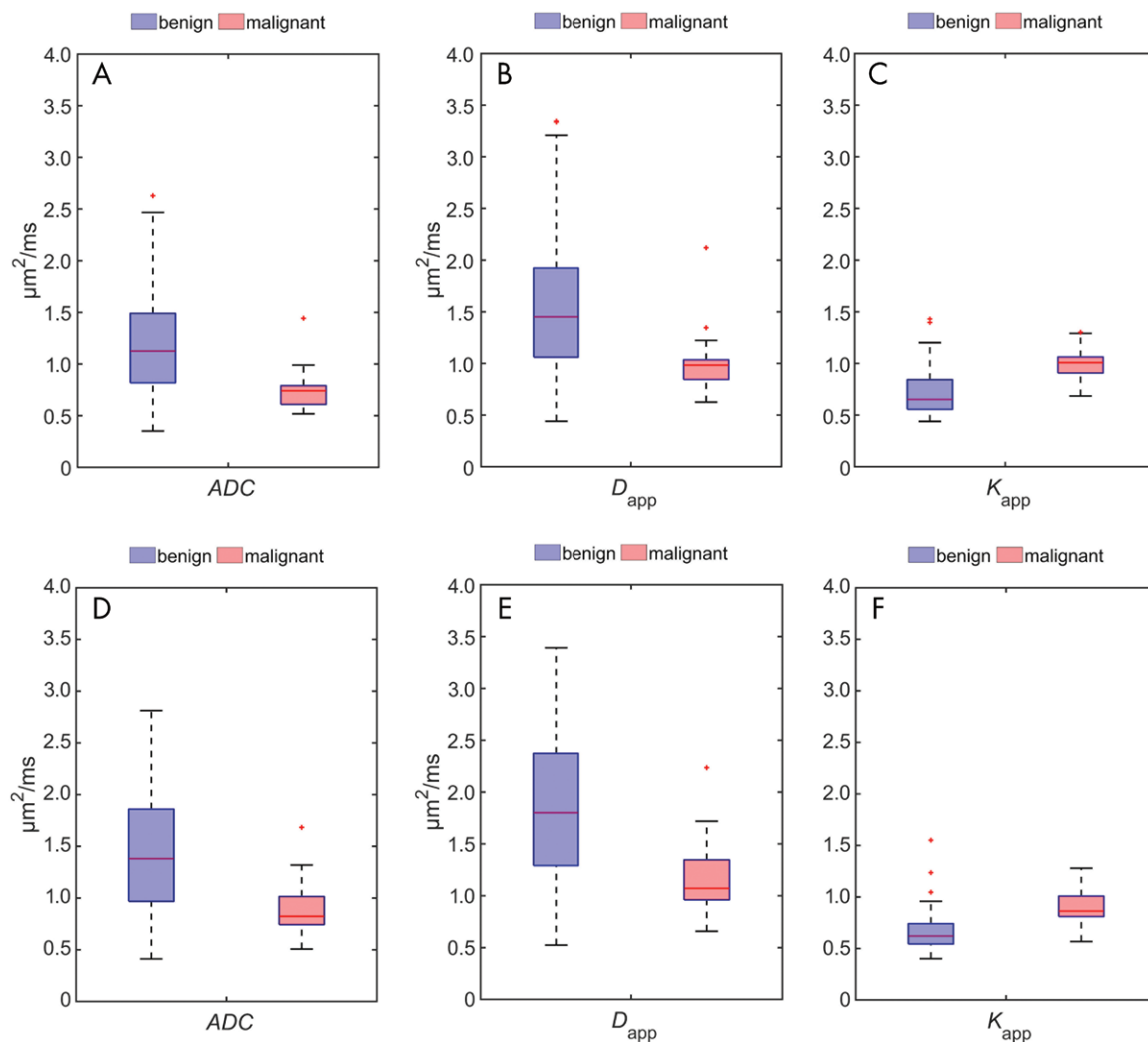


Figure 3: Box plots show, A–C, analysis of 1% of voxels and, D–F, analysis of 10% of voxels for, A, D, apparent diffusion coefficient (ADC) and two diffusion kurtosis MRI–derived variables, B, E, kurtosis-derived ADC (D_{app}) and, C, F, apparent kurtosis coefficient (K_{app}).

CI: 80.5%, 100%) malignant lesions were correctly classified as malignant. Fifty-one of 62 (82.3%; 95% CI: 70.5%, 90.8%) were correctly identified as benign, whereas the remaining 11 lesions (17.7%; 95% CI: 9.2%, 29.5%) were falsely assessed as malignant.

Adding Diffusion Kurtosis Imaging to Conventional MRI

The combination of conventional MRI and diffusion kurtosis MRI theoretically could have correctly classified 57 of 62 (91.9%; 95% CI: 82.2%, 97.3%) benign lesions, revealing seven of the 11 false-positive results.

The graphical presentation of the specificity for the different methods is shown in Figure 5.

Comparison of Different Methods

Statistical comparison of the specificity at 100% sensitivity level of our diffusion kurtosis analysis alone (55%) versus the specificity of the full diagnostic protocol (96.8%) by using McNemar test revealed significant difference ($P < .001$). Comparison of the full diagnostic protocol (specificity of 96.8%) versus

conventional MRI plus kurtosis results (specificity of 91.9%) revealed no statistical significant difference ($P > .05$).

Discussion

Discrimination of benign and malignant ovarian lesions preoperatively is of clinical importance for therapy decisions (1–3). Routine MRI protocols include a number of sequences including gadolinium-based contrast agent–enhanced sequences (8,40,41). Our study investigated the diagnostic performance of ultra-high- b -value diffusion kurtosis MRI in discriminating benign and malignant ovarian lesions. Our results suggest that at a sensitivity level of 100% (ie, not misclassifying malignant lesions), apparent kurtosis coefficient (K_{app}) correctly identifies 55% of benign lesions compared with 27% by using apparent diffusion coefficient (ADC) alone or 21% by using kurtosis-derived ADC (D_{app}) alone. Addition of diffusion kurtosis MRI to conventional MRI correctly classified 91.9% of benign lesions. With the addition of diffusion kurtosis MRI to the full diagnostic protocol including time-intensity curves, a correct classification of 96.8% was achieved.

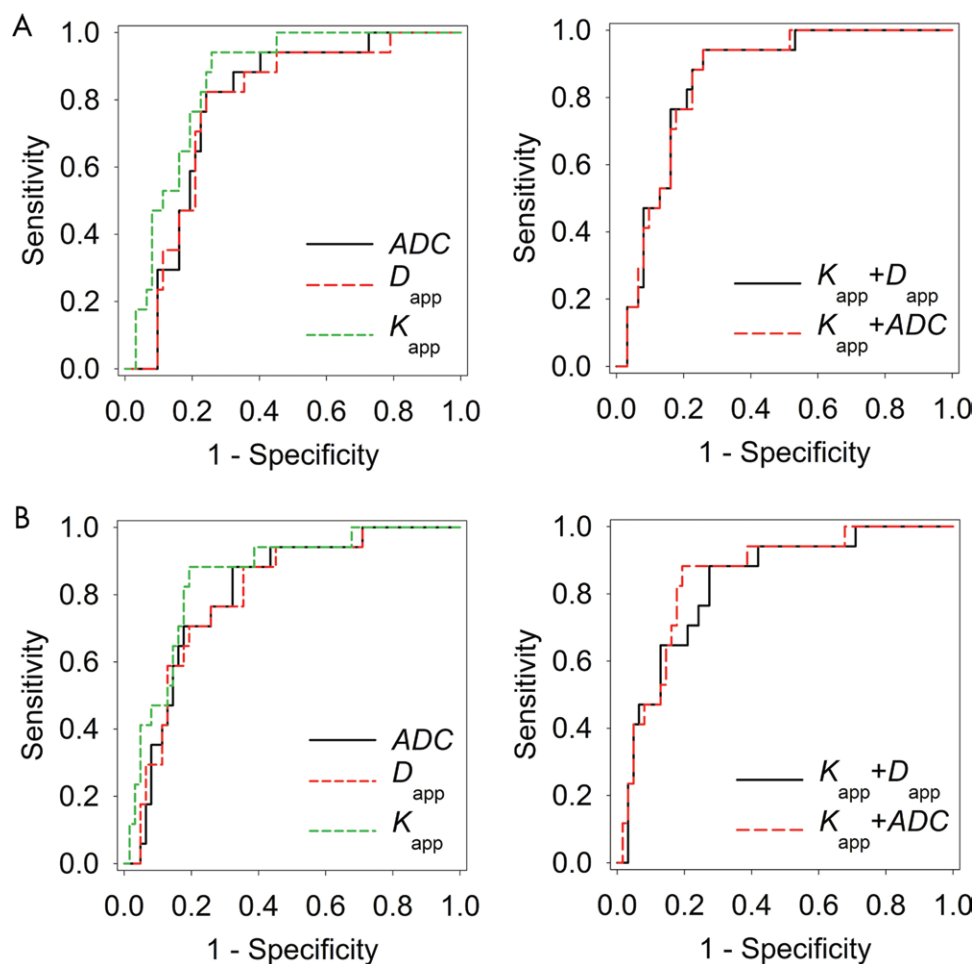


Figure 4: Graphs show, A, analysis of 1% of voxels and B, analysis of 10% of voxels. Left: Receiver operating characteristic (ROC) curves for mixed logistic model with single predictor [apparent diffusion coefficient [ADC], kurtosis-derived ADC [D_{app}], and apparent kurtosis coefficient [K_{app}]]. Right: ROC curves for mixed logistic model with two predictors (D_{app} and K_{app} and K_{app} and ADC).

To perform diffusion-weighted MRI in ovarian lesions is challenging. Two recent meta-analyses (42,43) found that mean quantitative ADC values could not reliably predict the nature of ovarian lesions. There is high tissue heterogeneity in ovarian lesions, often with cystic and different solid components, including fat and hemorrhage. Use of a mean value from the whole lesion seems counterintuitive as including cystic components produces high mean ADC values, masking the low diffusivity of any small malignant fraction. Therefore, our approach of framing the lesion, automatically selecting substructures for quantitative analysis, and using only those voxels with the highest diffusion restriction avoided the inclusion of falsely higher values in lesions with only small diffusion-restricted areas. Using only 1% of voxels within the drawn region of interest provided more reliable results compared with the usage of 10%, probably because in some lesions, the diffusion-restricted part was significantly smaller than 10% of the content of the region of interest.

The ADC values alone showed considerable overlap between benign and malignant lesions, which is in line with other studies comparing ADC values of malignant and benign lesions (20). If aiming to retain sensitivity of 100%, then we could only obtain a specificity of 27%. At a lower threshold of 88%, a specificity

of 68% was achieved. Additionally, fat components in benign lesions can impede the discriminative value of ADC.

The use of diffusion kurtosis MRI has shown advantages in tissue characterization as it examines non-Gaussian diffusion behaviors and better reflects microstructural complexity (19,44–46). Our results demonstrated that diffusion-weighted MRI and diffusion kurtosis MRI variables provide significantly different values between benign and malignant ovarian lesions. Combining K_{app} with D_{app} and K_{app} with ADC, respectively, did not significantly improve specificity.

A specificity of 76% at sensitivity level of 88% for K_{app} is superior to comparable data in the literature of conventional contrast-enhanced MRI stating specificity levels around 50%–60% at matching sensitivity levels. It is, depending on different studies, equal to or slightly inferior to published data of MRI including dynamic contrast-enhanced MRI with reported specificities of 74%–100% at sensitivity levels of 66%–100%. However, by combining T1-weighted, T2-weighted, and fat-saturated images and diffusion- and perfusion-weighted sequences, our results are inferior to published data with reported specificities of 81%–88% at sensitivity levels of 95%–100% (13–16). Also, our own analyses of the full diagnostic MRI protocol showed similar

Table 4: Summary of Diagnostic Performance of Diffusion and Kurtosis Diffusion Coefficients in Differentiating Malignant from Benign Ovarian Lesions

Variable	AUC	Specificity			
		Sensitivity of 100% (80, 100)	Sensitivity of 94% (71, 100)	Sensitivity of 88% (64, 99)	<i>P</i> Value*
1% analysis					
ADC	0.78 (0.67–0.89)	27 (17, 40)	60 (46, 72)	68 (55, 79)	.047
D_{app}	0.77 (0.66, 0.89)	21 (12, 33)	55 (42, 68)	65 (51, 76)	.05
K_{app}	0.85 (0.77, 0.94)	55 (42, 68)	74 (62, 84)	76 (63, 86)	...
K_{app} and D_{app}^{\dagger}	0.85 (0.77, 0.94)	47 (34, 60)	74 (62, 84)	77 (65, 87)	>.99
K_{app} and ADC [†]	0.85 (0.77, 0.94)	48 (36, 61)	74 (62, 84)	77 (65, 87)	.89
10% analysis					
GLMMIX parameters					
ADC	0.80 (0.70, 0.91)	29 (18, 42)	56 (43, 69)	68 (55, 79)	.06
D_{app}	0.80 (0.69, 0.91)	29 (18, 42)	55 (42, 68)	65 (51, 76)	.08
K_{app}	0.85 (0.75, 0.95)	32 (21, 45)	61 (48, 73)	81 (69, 90)	...
K_{app} and D_{app}^{\dagger}	0.83 (0.73, 0.94)	29 (18, 42)	58 (45, 70)	73 (60, 83)	.15
K_{app} and ADC [†]	0.85 (0.75, 0.95)	32 (21, 45)	61 (48, 73)	81 (69, 90)	... [‡]

Note.—Data in parentheses are 95% confidence intervals. ADC = apparent diffusion coefficient, AUC = area under receiver operating characteristic curve, D_{app} = kurtosis-derived ADC, GLMMIX = generalized linear mixed model, K_{app} = apparent kurtosis coefficient.

* P value for AUC comparison to AUC for K_{app} .

[†] Analysis using logistic mixed models with two predictors.

[‡] Fully identical curve characteristics; statistical comparison not operable.

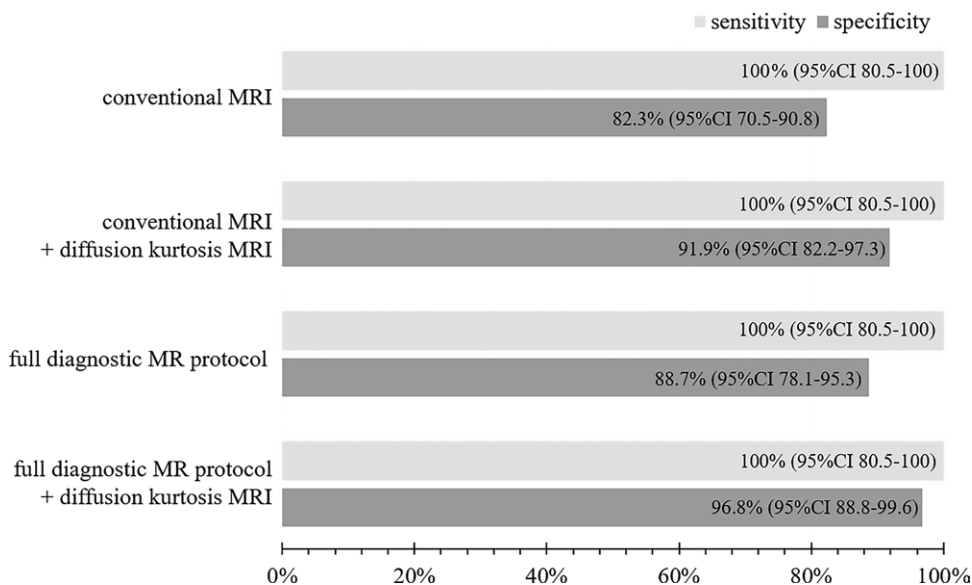


Figure 5: Graphical presentation of specificity at sensitivity level of 100% for different methods. CI = confidence interval.

sensitivity and specificity levels to published data of 100% and 89%. Addition of diffusion kurtosis MRI to conventional MRI without dynamic time-intensity curves improved our specificity from 82.3% to 91.1%, which then was not statistically significantly different from a full diagnostic protocol that included time-intensity curves. Addition of diffusion kurtosis to the full diagnostic protocol including time-intensity curves could have revealed additional five of the seven false-positive results as benign, resulting in specificity of 96.8% while preserving a

sensitivity of 100%. Thus, using diffusion kurtosis imaging might be promising for future diagnostic approaches, especially with the continuous concerns about potential gadolinium depositions after contrast medium administration (47–49), for patients with contraindications to gadolinium-based contrast agent administration and for the long-term goal to introduce quantitative imaging biomarkers for clinical diagnostics. Diffusion kurtosis imaging might also be promising considering the development of stepwise protocols, in terms of starting with noncontrast-enhanced scans and quantitative analyses and only administering

gadolinium-based contrast agents in those cases in which the unenhanced diffusion-weighted protocol might not already rule out malignancy.

Our study had several limitations. First, we only quantitatively analyzed diffusion on a single slice containing the highest diffusion restriction. Reassuringly, other studies comparing selected regions of interest with three-dimensional volumes found no significant advantage for three-dimensional volumes (50). Second, in the first reading round, radiologists involved

in clinical reading (including the full diagnostic protocol) had been included, potentially biasing the slice selection for the diffusion-weighted imaging reading round. However, a second independent read by a radiology resident, who had only diffusion-weighted and (for anatomic information) T2-weighted images available, did not provide significantly different AUCs. Third, we used only 1% or 10% of voxels within this region of interest for our final analysis because we aimed to include only the most suspicious part of the lesion. However, additional studies are warranted to assess optimal selection approaches for these highly heterogenic lesions. With regard to this aspect, by choosing those voxels with the most diffusion restriction automatically using the Matlab software, we ensured that the segmentation was not limited subjectively to a small diffusion-restricted volume of interest (51).

Fourth, we had a limited number of study participants, especially with malignant lesions; however, it is in the range of other studies investigating new techniques in MRI. Fifth, quantitative diffusion-weighted MRI variables might vary between scanners and the selected settings. Thus, the quantitative values described might not be simply transferred as reference to other imaging protocols and scanners. Sixth, the combination of the full diagnostic protocol and diffusion kurtosis imaging is a theoretical consideration because the kurtosis cutoff was generated from the same study cohort. Further prospective validation of the cutoff value will be required.

In conclusion, diffusion kurtosis MRI may have a role in MRI evaluation of sonographically indeterminate ovarian lesions prior to surgical procedure. Apparent kurtosis coefficient allowed better discrimination of benign ovarian lesions than did apparent diffusion coefficient alone, with 55% of benign lesions classified correctly at the sensitivity level of 100% for malignancy. Although performance of diffusion kurtosis MRI alone is inferior to the currently guideline-recommended standard MRI, it showed potential to match the current clinical standard when added to conventional MRI, and after further evaluation and technical standardization, may support radiologists especially when assessing ovarian lesions where gadolinium-based contrast agent cannot be administered.

Acknowledgment: The authors thank Tim Holland-Letz, Dr rer nat, for his statistical assistance with the manuscript.

Author contributions: Guarantors of integrity of entire study, T.M., P.S., H.P.S., J.R.; study concepts/study design or data acquisition or data analysis/interpretation, all authors; manuscript drafting or manuscript revision for important intellectual content, all authors; approval of final version of submitted manuscript, all authors; agrees to ensure any questions related to the work are appropriately resolved, all authors; literature research, T.M., M.W., C.D., P.S., R.G., H.U.K., H.P.S., J.R.; clinical studies, T.M., T.A.K., R.H., M.W., C.D., P.S., R.G., H.U.K., J.R., S.B.; experimental studies, T.A.K., P.S., R.G., J.R.; ; statistical analysis, T.M., A.M.B., P.S., J.R.; and manuscript editing, T.M., A.M.B., T.A.K., F.C.H., M.W., C.D., J.B., P.S., R.G., H.U.K., H.P.S., J.R., S.B.

Disclosures of Conflicts of Interest: T.M. disclosed no relevant relationships. A.M.B. disclosed no relevant relationships. T.A.K. disclosed no relevant relationships. F.C.H. disclosed no relevant relationships. R.H. disclosed no relevant relationships. M.W. disclosed no relevant relationships. C.D. disclosed no relevant relationships. J.B. disclosed no relevant relationships. P.S. disclosed no relevant relationships. R.G. disclosed no relevant relationships. H.U.K. Activities related to the present article: disclosed no relevant relationships. Activities not related to the present article: has grants/grants pending with Bayer, Philips, and Siemens;

received payment for lectures including service on speakers bureaus from Astra-Zeneca, Boehringer Ingelheim, Merck Sharp Dome, and Philips. Other relationships: disclosed no relevant relationships. H.P.S. Activities related to the present article: disclosed no relevant relationships. Activities not related to the present article: received payment for lectures including service on speakers bureaus from Bayer, Curagita, and Siemens. Other relationships: disclosed no relevant relationships. J.R. disclosed no relevant relationships. S.B. Activities related to the present article: disclosed no relevant relationships. Activities not related to the present article: has grants/grants pending with nonprofit organizations; received payment for lectures including service on speakers bureaus from Siemens Healthineers; has patents pending in the field of diffusion-weighted imaging. Other relationships: disclosed no relevant relationships.

References

- Vernooij F, Heintz P, Witteveen E, van der Graaf Y. The outcomes of ovarian cancer treatment are better when provided by gynecologic oncologists and in specialized hospitals: a systematic review. *Gynecol Oncol* 2007;105(3):801–812.
- Cannistra SA. Cancer of the ovary. *N Engl J Med* 2004;351(24):2519–2529.
- Choi JI, Park SB, Han BH, et al. Imaging features of complex solid and multicystic ovarian lesions: proposed algorithm for differential diagnosis. *Clin Imaging* 2016;40(1):46–56.
- Timmerman D, Van Calster B, Testa AC, et al. Ovarian cancer prediction in adnexal masses using ultrasound-based logistic regression models: a temporal and external validation study by the IOTA group. *Ultrasound Obstet Gynecol* 2010;36(2):226–234.
- Rieber A, Nüssle K, Stöhr I, et al. Preoperative diagnosis of ovarian tumors with MR imaging: comparison with transvaginal sonography, positron emission tomography, and histologic findings. *AJR Am J Roentgenol* 2001;177(1):123–129.
- Timmerman D, Ameye L, Fischerova D, et al. Simple ultrasound rules to distinguish between benign and malignant adnexal masses before surgery: prospective validation by IOTA group. *BMJ* 2010;341:c6839.
- Timmerman D, Schwärzler P, Collins WP, et al. Subjective assessment of adnexal masses with the use of ultrasonography: an analysis of interobserver variability and experience. *Ultrasound Obstet Gynecol* 1999;13(1):11–16.
- Forstner R, Thomassin-Naggara I, Cunha TM, et al. ESUR recommendations for MR imaging of the sonographically indeterminate adnexal mass: an update. *Eur Radiol* 2017;27(6):2248–2257 [Published correction appears in *Eur Radiol* 2017;27(6):2258.].
- Kinkel K, Lu Y, Mehdizade A, Pelte MF, Hricak H. Indeterminate ovarian mass at US: incremental value of second imaging test for characterization—meta-analysis and Bayesian analysis. *Radiology* 2005;236(1):85–94.
- Chen M, Wang WC, Zhou C, et al. Differentiation between malignant and benign ovarian tumors by magnetic resonance imaging. *Chin Med Sci J* 2006;21(4):270–275.
- Sohaib SA, Sahdev A, Van Trappen P, Jacobs IJ, Reznick RH. Characterization of adnexal mass lesions on MR imaging. *AJR Am J Roentgenol* 2003;180(5):1297–1304.
- Hricak H, Chen M, Coakley FV, et al. Complex adnexal masses: detection and characterization with MR imaging—multivariate analysis. *Radiology* 2000;214(1):39–46.
- Thomassin-Naggara I, Toussaint I, Perrot N, et al. Characterization of complex adnexal masses: value of adding perfusion- and diffusion-weighted MR imaging to conventional MR imaging. *Radiology* 2011;258(3):793–803.
- Bernardin L, Dilks P, Liyanage S, Miquel ME, Sahdev A, Rockall A. Effectiveness of semi-quantitative multiphase dynamic contrast-enhanced MRI as a predictor of malignancy in complex adnexal masses: radiological and pathological correlation. *Eur Radiol* 2012;22(4):880–890.
- Dilks P, Narayanan P, Reznick R, Sahdev A, Rockall A. Can quantitative dynamic contrast-enhanced MRI independently characterize an ovarian mass? *Eur Radiol* 2010;20(9):2176–2183.
- Mohaghegh P, Rockall AG. Imaging strategy for early ovarian cancer: characterization of adnexal masses with conventional and advanced imaging techniques. *RadioGraphics* 2012;32(6):1751–1773.
- Fujii S, Kakite S, Nishihara K, et al. Diagnostic accuracy of diffusion-weighted imaging in differentiating benign from malignant ovarian lesions. *J Magn Reson Imaging* 2008;28(5):1149–1156.
- American College of Radiology. ACR Appropriateness Criteria: Clinically Suspected Adnexal Mass, No Acute Symptoms. <https://acsearch.acr.org/docs/69466/Narrative/>. Published 2018. Accessed January 31, 2020.
- Qi XX, Shi DF, Ren SX, et al. Histogram analysis of diffusion kurtosis imaging derived maps may distinguish between low and high grade gliomas before surgery. *Eur Radiol* 2018;28(4):1748–1755.

20. Jiang JX, Tang ZH, Zhong YF, Qiang JW. Diffusion kurtosis imaging for differentiating between the benign and malignant sinonasal lesions. *J Magn Reson Imaging* 2017;45(5):1446–1454.
21. Si Y, Liu RB. Diagnostic Performance of Monoexponential DWI Versus Diffusion Kurtosis Imaging in Prostate Cancer: A Systematic Review and Meta-Analysis. *AJR Am J Roentgenol* 2018;211(2):358–368.
22. Wen Z, Chen Y, Yang X, et al. Application of magnetic resonance diffusion kurtosis imaging for distinguishing histopathologic subtypes and grades of rectal carcinoma. *Cancer Imaging* 2019;19(1):8.
23. Jensen JH, Helpern JA, Ramani A, Lu H, Kaczynski K. Diffusional kurtosis imaging: the quantification of non-gaussian water diffusion by means of magnetic resonance imaging. *Magn Reson Med* 2005;53(6):1432–1440.
24. Bickelhaupt S, Jaeger PF, Laun FB, et al. Radiomics Based on Adapted Diffusion Kurtosis Imaging Helps to Clarify Most Mammographic Findings Suspicious for Cancer. *Radiology* 2018;287(3):761–770.
25. Qi C, Yang S, Meng L, et al. Evaluation of cerebral glioma using 3T diffusion kurtosis tensor imaging and the relationship between diffusion kurtosis metrics and tumor cellularity. *J Int Med Res* 2017;45(4):1347–1358.
26. Fritzsche KH, Neher PF, Reicht I, et al. MITK diffusion imaging. *Methods Inf Med* 2012;51(5):441–448.
27. Le Bihan D, Breton E, Lallemand D, Grenier P, Cabanis E, Laval-Jeantet M. MR imaging of intravoxel incoherent motions: application to diffusion and perfusion in neurologic disorders. *Radiology* 1986;161(2):401–407.
28. Xu XQ, Hu H, Su GY, et al. Utility of histogram analysis of ADC maps for differentiating orbital tumors. *Diagn Interv Radiol* 2016;22(2):161–167.
29. Zhang W, Zhou Y, Xu XQ, et al. A Whole-Tumor Histogram Analysis of Apparent Diffusion Coefficient Maps for Differentiating Thymic Carcinoma from Lymphoma. *Korean J Radiol* 2018;19(2):358–365.
30. Suo S, Zhang K, Cao M, et al. Characterization of breast masses as benign or malignant at 3.0T MRI with whole-lesion histogram analysis of the apparent diffusion coefficient. *J Magn Reson Imaging* 2016;43(4):894–902.
31. Bougias H, Ghiatas A, Priovolos D, Veliou K, Christou A. Whole-lesion histogram analysis metrics of the apparent diffusion coefficient as a marker of breast lesions characterization at 1.5 T. *Radiography (Lond)* 2017;23(2):e41–e46.
32. Chen Y, Wu B, Liu H, Wang D, Gu Y. Feasibility study of dual parametric 2D histogram analysis of breast lesions with dynamic contrast-enhanced and diffusion-weighted MRI. *J Transl Med* 2018;16(1):325.
33. Wu X, Reinikainen P, Vanhanen A, et al. Correlation between apparent diffusion coefficient value on diffusion-weighted MR imaging and Gleason score in prostate cancer. *Diagn Interv Imaging* 2017;98(1):63–71.
34. Sjöholm T, Ekström S, Strand R, et al. A whole-body FDG PET/MR atlas for multiparametric voxel-based analysis. *Sci Rep* 2019;9(1):6158.
35. Maani R, Yang YH, Kalra S. Voxel-based texture analysis of the brain. *PLoS One* 2015;10(3):e0117759.
36. Jensen JH, Helpern JA. MRI quantification of non-Gaussian water diffusion by kurtosis analysis. *NMR Biomed* 2010;23(7):698–710.
37. Nogueira L, Brandão S, Matos E, et al. Application of the diffusion kurtosis model for the study of breast lesions. *Eur Radiol* 2014;24(6):1197–1203.
38. Giannelli M, Toschi N. On the use of trace-weighted images in body diffusional kurtosis imaging. *Magn Reson Imaging* 2016;34(4):502–507.
39. Koo TK, Li MY. A Guideline of Selecting and Reporting Intraclass Correlation Coefficients for Reliability Research. *J Chiropr Med* 2016;15(2):155–163 [Published correction appears in *J Chiropr Med* 2017;16(4):346.].
40. Kanda T, Oba H, Toyoda K, Kitajima K, Furui S. Brain gadolinium deposition after administration of gadolinium-based contrast agents. *Jpn J Radiol* 2016;34(1):3–9.
41. Deike-Hofmann K, Reuter J, Haase R, et al. Glymphatic Pathway of Gadolinium-Based Contrast Agents Through the Brain: Overlooked and Misinterpreted. *Invest Radiol* 2019;54(4):229–237.
42. Pi S, Cao R, Qiang JW, Guo YH. Utility of DWI with quantitative ADC values in ovarian tumors: a meta-analysis of diagnostic test performance. *Acta Radiol* 2018;59(11):1386–1394.
43. Kim HJ, Lee SY, Shin YR, Park CS, Kim K. The Value of Diffusion-Weighted Imaging in the Differential Diagnosis of Ovarian Lesions: A Meta-Analysis. *PLoS One* 2016;11(2):e0149465.
44. Sui Y, Wang H, Liu G, et al. Differentiation of Low- and High-Grade Pediatric Brain Tumors with High b-Value Diffusion-weighted MR Imaging and a Fractional Order Calculus Model. *Radiology* 2015;277(2):489–496.
45. Partridge SC, Nissan N, Rahbar H, Kitsch AE, Sigmund EE. Diffusion-weighted breast MRI: Clinical applications and emerging techniques. *J Magn Reson Imaging* 2017;45(2):337–355.
46. Tang L, Zhou XJ. Diffusion MRI of cancer: From low to high b-values. *J Magn Reson Imaging* 2019;49(1):23–40.
47. Blumfield E, Swenson DW, Iyer RS, Stancescu AL. Gadolinium-based contrast agents - review of recent literature on magnetic resonance imaging signal intensity changes and tissue deposits, with emphasis on pediatric patients. *Pediatr Radiol* 2019;49(4):448–457.
48. Guo BJ, Yang ZL, Zhang LJ. Gadolinium Deposition in Brain: Current Scientific Evidence and Future Perspectives. *Front Mol Neurosci* 2018;11:335.
49. Lyapustina T, Goldfine C, Rhyee S, Babu KM, Griswold MK. Evaluating the Patient with Reported Gadolinium-Associated Illness. *J Med Toxicol* 2019;15(1):36–44.
50. Tamada T, Huang C, Ream JM, Taffel M, Taneja SS, Rosenkrantz AB. Apparent Diffusion Coefficient Values of Prostate Cancer: Comparison of 2D and 3D ROIs. *AJR Am J Roentgenol* 2018;210(1):113–117.
51. Padhani AR, Liu G, Koh DM, et al. Diffusion-weighted magnetic resonance imaging as a cancer biomarker: consensus and recommendations. *Neoplasia* 2009;11(2):102–125.